12th International Symposium on Turbulence and Shear Flow Phenomena (TSFP12)
Osaka, Japan (Online), July 19-22, 2022

DNS STUDY OF TURBULENT FLOW IN A CIRCULAR PIPE SUBJECTED TO AXIAL SYSTEM ROTATION

Zhao-Ping Zhang
Department of Mechanical Engineering
University of Manitoba
Winnipeg, MB, R3T 5V6, Canada
umzha258@myumanitoba.ca

Bing-Chen Wang
Department of Mechanical Engineering
University of Manitoba
Winnipeg, MB, R3T 5V6, Canada
BingChen.Wang@umanitoba.ca

ABSTRACT

Turbulent circular pipe flows under axial system rotation are investigated using direct numerical simulation (DNS) for a wide range of rotation numbers of $Ro_b = 0-20$. The characteristics of the flow field are investigated in both physical and spectral spaces. It is observed that large-scale secondary flows are induced by the axial rotation, which enhance the magnitudes of the radial and azimuthal Reynolds normal stresses. In response to the axial system rotation imposed, the pressure-strain and Coriolis production terms become the leading terms in the budget balance of these two Reynolds normal stresses. It is also interesting to observe that the axial rotation makes the near-wall streaky structures tilted and elongated, and suppresses the sweep events systematically which further impede the formation of hairpin structures.

INTRODUCTION

Turbulent flow within a circular pipe subjected to system rotation represents an interesting topic with important applications in areas such as internal blade cooling of gas turbines, and rotary machines. The system rotation of the circular pipe may occur either radially about a diameter of the pipe, or axially about the centre line of the pipe. In response to either radial or axial system rotation, Coriolis force is induced which acts on the fluid flows to dramatically alter the turbulence statistics and coherent structures, even resulting in local laminarization of the flow. As is well known, turbulent flow through a stationary (non-rotating) circular pipe represents a classical research subject, which has been extensively studied using DNS by Eggels *et al.* (1994); Wu & Moin (2008); Chin *et al.* (2010). By contrast, the number of DNS studies on either radially and axially rotating circular pipe flows are still very limited in the literature. Recently, Zhang & Wang (2019) carried out a DNS study of turbulent flow in a circular pipe subjected to radial system rotation. They observed streamwise-elongated large-scale counter-rotating vortices and a Taylor-Proudman region at low rotation numbers. Following our previous DNS study of radially-rotating pipe flow, here we extend the research to DNS of axially-rotating pipe flows.

In their series of rotating pipe experiments, Reich & Beer (1989) observed that both skin friction coefficient and turbulence level decreased considerably as the rotation number increased. Meanwhile, according to the trend of the mean axial velocity profile, the flow became increasingly laminarized with an increasing speed of axial system rotation. Orlandi & Fatica (1997) carried out a DNS study of an axially-rotating circular pipe flow, and confirmed these experimental research findings of Reich & Beer (1989). They also observed that the turbulence statistics were sensitive to the tilting of the near-wall axial vortical structures in the rotating direction. Orlandi & Ebstein (2000) further studied the impact of axial system rotation on the budget balances of TKE, Reynolds stresses and enstrophy of the turbulent pipe flow using DNS. They reported that for the Reynolds stresses, the pressure-strain and convection terms were highly dependent on the rotation number.

Based on a thorough literature review, it is noticed that detailed DNS studies of the axial-rotating circular pipe flow are still rather limited, and in-depth understanding of the Coriolis force effects on the flow physics and coherent structures needs to be developed. In view of this, we aim to conduct a systematic DNS study of turbulent pipe flows subjected to axial system rotation for a wide range of rotation numbers.

TEST CASE AND NUMERICAL ALGORITHM

Figure 1 schematically illustrates a circular pipe under axial system rotation. Three directions of the cylindrical coordinates (i.e. radial, azimuthal and axial directions) are denoted as r, β and z, and the corresponding velocity components are represented as u_r, u_β and u_z, respectively. The pipe length is $L_z = 30\pi R$, where R is the pipe radius. The flow field in the domain is fully developed with a periodic boundary condition applied to the axial direction and no-slip condition imposed on the solid surface. In order to study the axially-rotating effect, a constant counter-clockwise angular speed (Ω_z) is imposed in the streamwise (z) direction, and the rotation number ($Ro_b = 2\Omega_z R/U_b$) ranges drastically from 0 (non-rotating case) to 20, at a fixed Reynolds number of $Re_\tau = u_\tau R/\nu = 180$. Here, U_b is the bulk mean velocity, u_τ is the wall friction velocity, and ν is the kinematic viscosity of the fluid. The governing equations for an incompressible flow with respect to an axially-rotating reference frame are

$$\nabla \cdot \vec{u} = 0 \quad , \tag{1}$$

$$\frac{\partial \vec{u}}{\partial t} + \vec{u} \cdot \nabla \vec{u} = -\Pi \hat{\mathbf{e}}_z - \frac{1}{\rho}\nabla p + \nu \nabla^2 \vec{u} + \vec{F} \quad , \tag{2}$$

where $\vec{u}$, ρ and p are the velocity, density and pressure of the fluid, respectively. Π represents the constant mean axial pressure gradient, and $\hat{e}_z$ is the base unit vector of the z-direction, with $|\hat{e}_z| \equiv 1$. In response to the axial rotation, two components of the Coriolis force ($\vec{F}$) appear in the radial and azimuthal directions, i.e. $F_r = 2\Omega_z u_\beta$ and $F_\beta = -2\Omega_z u_r$.

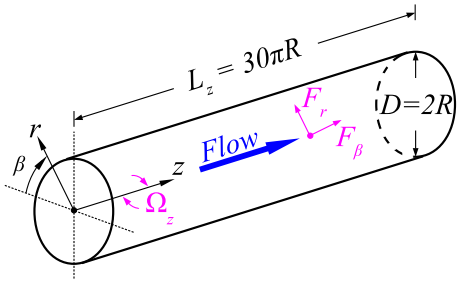

Figure 1. Schematic of turbulent pipe flow subjected to axial system rotation in cylindrical coordinate system. Two Coriolis force components are F_r and F_β.

Table 1. Flow parameters for seven test cases.

Case #	Ω_z	Ro_b	Ro_b^A	Ro_τ^A	Re_τ^A
1	0	0	0	0	179.94
2	1	2	1.83	29.47	179.84
3	2	4	3.67	58.86	180.09
4	3	6	5.53	88.38	179.91
5	5	10	9.79	147.41	179.77
6	7	14	14.95	206.15	179.96
7	10	20	22.45	295.72	179.22

The simulations were performed with a spectral-element code "Semtex" by Blackburn & Sherwin (2004), which is highly-accurate in algorithm suitable for conducing DNS. It was developed using C++ programming language, and parallelized following the message passing interface (MPI) standard. For the mesh, a quadrilateral spectral-element method was used to divide the cross-section of the pipe into 420 elements with each element discretized spatially with 8th-order Gauss-Lobatto-Legendre Lagrange interpolants. All physical quantities are expanded into the spectral space using Fourier series with 1800 modes in the z-direction. The grid spacing is uniform in the streamwise direction with $\Delta z^+ = 9.425$, and varies in the azimuthal and radial directions with $R\Delta\beta^+ = 1.416\text{-}5.122$, $\Delta r^+ = 0.147$ at the first node off the wall and $\Delta r^+ = 0.942$ at the pipe centre.

Table 1 compares the nominal and actual flow parameters derived from DNS results of the different test cases. Superscript "A" denotes the actual results. Ro_τ represents rotation number defined based on the wall friction velocity as $Ro_\tau = 2\Omega_z R/u_\tau$. For each simulated case, 500 instantaneous snapshots of the flow fields over 40 large-eddy turnover times (LETOTs, defined as R/u_τ) were collected with approximately 1.1 TB data stored on a server. Here, u_τ is defined as $\sqrt{-\Pi R/2\rho}$. All DNS calculations were conducted on the WestGrid (Western Canada Research Grid) supercomputers.

To facilitate the analysis and discussion, an instantaneous turbulence variable Φ is decomposed as $\Phi = \langle\Phi\rangle + \Phi'$ where $\langle\Phi\rangle$ is the temporal- and spatial-averaging component along the homogenous (z) direction, and Φ' represents fluctuating component. Symbol y denotes a dimensionless coordinate measured from the wall, i.e. $y = 1 - r/R$. Furthermore, in order to conduct a near-wall analysis in analogous to a turbulent plane channel flow, a dimensionless wall coordinate is introduced, i.e. $y^+ = (R-r)u_\tau/\nu$.

RESULTS AND DISCUSSIONS

Figure 2 shows contours of the instantaneous axial velocity u_z^+ and instantaneous axial vorticity ω_z^+ in the cross-stream plane for the non-rotating ($Ro_b = 0$) and most rapidly-rotating ($Ro_b = 20$) flows. The left panel shows the instantaneous axial velocity u_z^+, while the right part shows the instantaneous axial vorticity ω_z^+. As is clear from Fig. 2(a), in a non-rotating pipe flow, the flow structures show "mushroom patterns" in the near-wall region where several couples of small counter-rotating vorticities are observed. In Fig. 2(b), as the rotating speed increases to $Ro_b = 20$, a large rotating vortical structure appears at the pipe centre, and both the "mushroom patterns" and vorticities are stretched along the azimuthal direction.

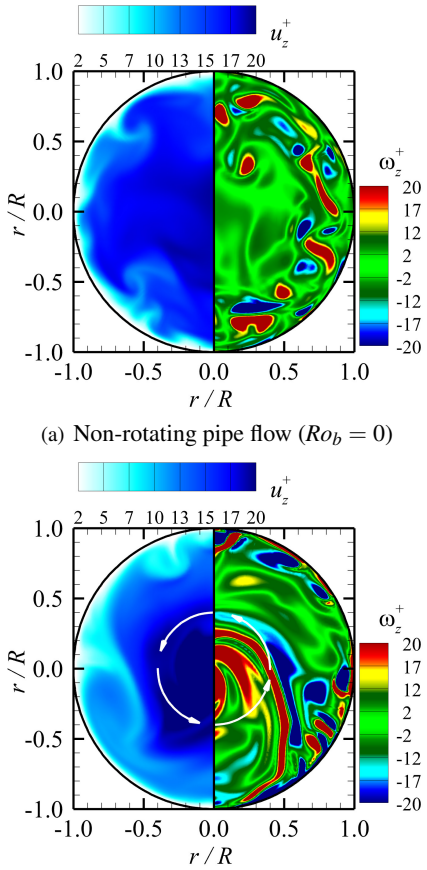

(a) Non-rotating pipe flow ($Ro_b = 0$)

(b) Axially-rotating pipe flow ($Ro_b = 20$)

Figure 2. Cross-stream distribution of instantaneous axial velocity u_z^+ (left half-panel) and instantaneous axial vorticity ω_z^+ (right half-panel) of the non-rotating ($Ro_b = 0$) and most rapidly-rotating ($Ro_b = 20$) flows. White Arrows represent the counter-clockwise-rotating direction. All contours are mapped at the same axial location ($z/R = 15\pi$) and time instant (20.38 LETOTs). All values are non-dimensionalized by u_τ.

Figure 3 compares bulk mean velocity U_b^+ and volume-averaged TKE k_m^+ of different rotation numbers Ro_b. In Fig. 3(a), the U_b^+ profile peaks at $Ro_b = 2$, with a magnitude that is 10.01% higher than that of the non-rotating pipe flow. As the rotation number increases beyond 6, the magnitude of U_b^+ decreases apparently. Finally, at $Ro_b = 20$, the U_b^+ value is reduced by 10.33% in comparison with that of the non-rotating flow. From Fig. 3(b), The value of k_m^+ increases as the rotation number increases, and reaches its maximum at $Ro_b = 14$. It will be explained later that the axial rotation enhances the magnitudes of $\langle u_z' u_z'\rangle^+$ and $\langle u_\beta' u_\beta'\rangle^+$ which subsequently make a positive contribution to the k_m^+ value.

Figure 4 compares the profiles of the mean axial velocity $\langle u_z\rangle^+$, mean azimuthal velocity $r\langle u_\beta\rangle^+/R$ and mean axial vorticity $\langle\omega_z\rangle^+$ with respect to the wall-normal distance (y) of all seven rotation numbers tested. As is evident from Fig. 4(a), the $\langle u_z\rangle^+$ profile is axial-symmetrical for the non-rotating pipe flow, and varies non-monotonically with an increasing Ro_b

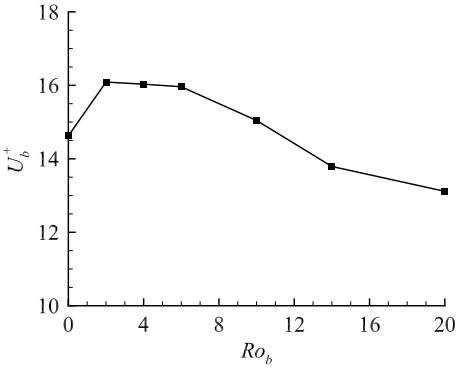

(a) Bulk mean velocity U_b^+

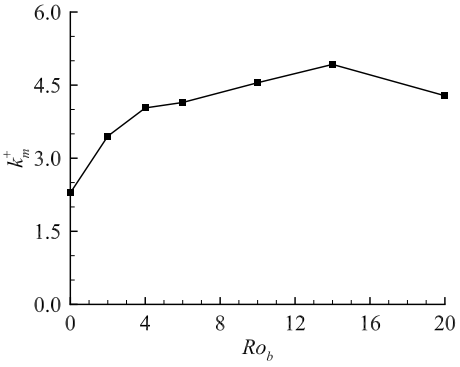

(b) Volume-averaged TKE k_m^+

Figure 3. Profiles of bulk mean velocity U_b^+ and volume-averaged TKE k_m^+ with respect to the rotation number Ro_b. The values of U_b^+ and k_m^+ have been non-dimensionalized by u_τ and u_τ^2, respectively.

value. At the pipe centre, the peak value of $\langle u_z\rangle^+$ increases when rotating speed rises from $Ro_b = 0$ to 6, and reaches its maximum at $Ro_b = 6$ with a magnitude that is 40.05% higher than that of the non-rotating pipe flow. As Ro_b increases from 6 to 20, the peak value of $\langle u_z\rangle^+$ reduces, which however is still 18.48% larger than that at $Ro_b = 0$. In addition, it is interesting to observe from Figs. 4(b) and (c) that both $r\langle u_\beta\rangle^+/R$ and $\langle \omega_z\rangle^+$ reach their maxima at $Ro_b = 10$, and the peak of $r\langle u_\beta\rangle^+/R$ is always located around $y \approx 0.4$ where the mean axial vorticity $\langle \omega_z\rangle^+$ is zero identically.

Figure 5 compares the profiles of Reynolds normal stresses $\langle u_z'u_z'\rangle^+$, $\langle u_r'u_r'\rangle^+$ and $\langle u_\beta'u_\beta'\rangle^+$ at seven different rotation numbers Ro_b tested. As shown in Fig. 5(a), the profile of $\langle u_z'u_z'\rangle^+$ peaks at $y = 0.083$ (or $y^+ \approx 15$) in the near-wall region for a non-rotating pipe flow. As soon as the axial rotation is imposed, the magnitude of $\langle u_z'u_z'\rangle^+$ reduces monotonically. In response to the effect of the mean secondary flow, the peak of $\langle u_z'u_z'\rangle^+$ moves towards the pipe centre as Ro_b increases. The lowest and highest peak values occur at $Ro_b = 4$ and $Ro_b = 14$, respectively, which are 15.77% and 6.87% lower than that of the non-rotating pipe flow (at $Ro_b = 0$).

As is clear in Fig. 5(b), in contrast to the monotonic trend of $\langle u_r'u_r'\rangle^+$ in the near-wall region of the pipe, the profile of $\langle u_r'u_r'\rangle^+$ varies non-monotonically at the pipe centre as the rotation number increases, and reaches its maximum at $Ro_b = 14$. Figure 5(c) shows that the profile of $\langle u_\beta'u_\beta'\rangle^+$ is similar to that of $\langle u_r'u_r'\rangle^+$ in the azimuthal direction, with the maximum peak also occurring at $Ro_b = 14$. In response to the system rotation imposed, the secondary flows are induced, which tend to suppress $\langle u_z'u_z'\rangle^+$ but enhance the magnitudes of $\langle u_r'u_r'\rangle^+$ and $\langle u_\beta'u_\beta'\rangle^+$ in most pipe regions until the rotation number reaches $Ro_b = 14$. As a result, the TKE level (as

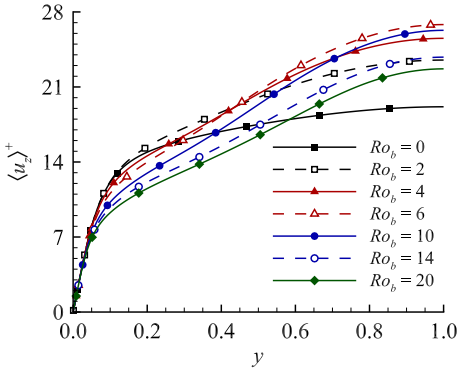

(a) Mean axial velocity $\langle u_z\rangle^+$

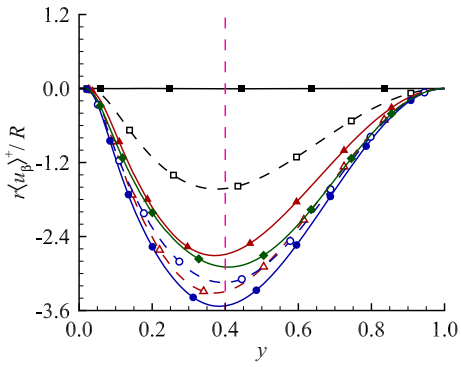

(b) Mean azimuthal velocity $r\langle u_\beta\rangle^+/R$

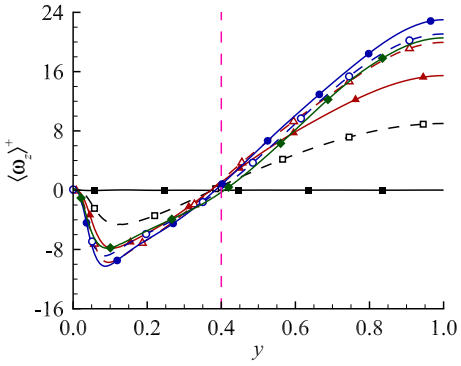

(c) Mean axial vorticity $\langle \omega_z\rangle^+$

Figure 4. Profiles of mean axial velocity $\langle u_z\rangle^+$, mean azimuthal velocity $r\langle u_\beta\rangle^+/R$ and mean axial vorticity $\langle \omega_z\rangle^+$ at seven tested rotation numbers. In panels (b) and (c), pink vertical-dashed lines point to the location of zero $\langle \omega_z\rangle^+$ at $y = 0.4$. All values have been non-dimensionalized by u_τ.

shown in Fig. 3(b)) is enhanced significantly. As Ro_b increases above 14, the magnitudes of $\langle u_r'u_r'\rangle^+$ and $\langle u_\beta'u_\beta'\rangle^+$ decrease with Ro_b, leading to a reduction in the TKE level.

Figure 6 compares the profiles of axial pre-multiplied velocity spectrum $k_z^+\widetilde{E}_{zz}^+$ calculated along the streamwise direction at wall-normal position $y^+ \approx 15$. The 1D axial energy spectrum of velocity fluctuations is defined as

$$\widetilde{E}_{ij} = \overline{\widehat{u_i'}\widehat{u_j'}^* + \widehat{u_i'}^*\widehat{u_j'}} \quad , \tag{3}$$

where a hat denotes Fourier transform and an overbar represents time averaging. The axial wavenumber is determined as $k_z = n_z k_{z0}$ for $n_z \in$ [-N_z/2, N_z/2-1] where $k_{z0} = 2\pi/L_z$ is the smallest positive wavenumber. The axial wavelength is defined as $\lambda_z = 2\pi/k_z$, non-dimensionalized as $\lambda_z^+ = \lambda_z u_\tau/\nu$.

As is evident from Fig. 6, the mode of $k_z^+\widetilde{E}_{zz}^+$ (corresponding to the characteristic length scale of the most energetic eddies) is located in the region of $\lambda_z^+ \in$ [600, 2000] for a non-

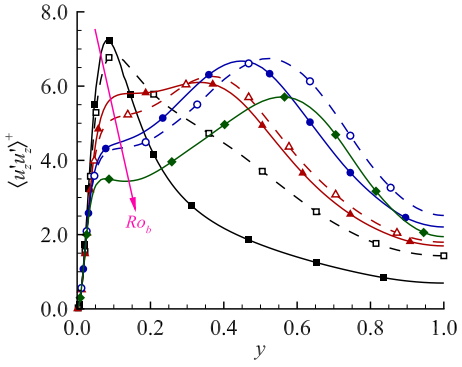

(a) Axial Reynolds normal stress $\langle u_z' u_z' \rangle^+$

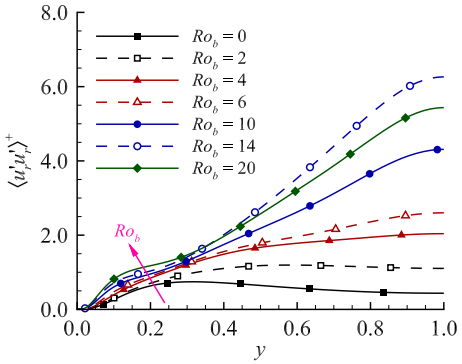

(b) Radial Reynolds normal stress $\langle u_r' u_r' \rangle^+$

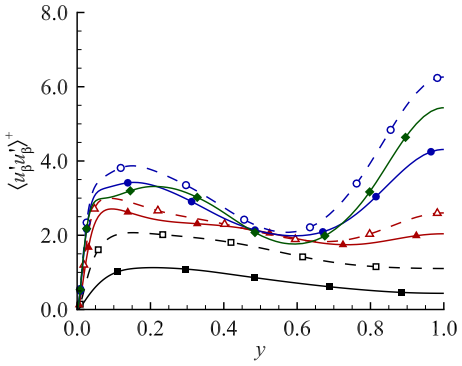

(c) Azimuthal Reynolds normal stress $\langle u_\beta' u_\beta' \rangle^+$

Figure 5. Profiles of Reynolds normal stresses $\langle u_z' u_z' \rangle^+$, $\langle u_r' u_r' \rangle^+$ and $\langle u_\beta' u_\beta' \rangle^+$ for different rotation numbers Ro_b. In panels (a) and (b), pink arrows point to the direction of an increasing rotating effect. All values are non-dimensionalized by u_τ^2.

rotating pipe flow. In response to the axial system rotation, the peak value decreases dramatically as Ro_b increases. At the highest rotation number $Ro_b = 20$, the magnitude is reduced by 63.02% in comparison with that at $Ro_b = 0$. Meanwhile, the mode of $k_z^+ \widetilde{E}_{zz}^+$ moves towards larger wavelengths as the rotation number increases.

To refine our investigation of the rotating impact on the Reynolds normal stresses, the transport equation of Reynolds stresses $\langle u_i' u_j' \rangle$ can be further studied, which is expressed as

$$H_{ij} - P_{ij} - \Pi_{ij} + \varepsilon_{ij} - D_{ij}^t - D_{ij}^p - D_{ij}^v - C_{ij} = 0 \quad . \qquad (4)$$

Here, H_{ij}, P_{ij}, Π_{ij}, ε_{ij}, D_{ij}^t, D_{ij}^p, D_{ij}^v and C_{ij} represent the convection, production, pressure-strain, viscous dissipation, turbulent diffusion, pressure diffusion, viscous diffusion and Coriolis production terms, respectively. From Fig. 1, it is understood that the two components of the Coriolis force are in the radial and azimuthal directions under the axial rotation. Because no Coriolis force component appears in the

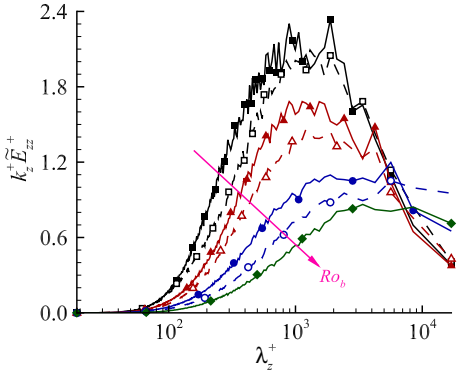

Figure 6. Profile of axial pre-multiplied velocity spectrum $k_z^+ \widetilde{E}_{zz}^+$ for 7 different rotation numbers, calculated along the streamwise direction at wall-normal position $y^+ \approx 15$. Pink arrow indicates the direction of an increasing rotation number.

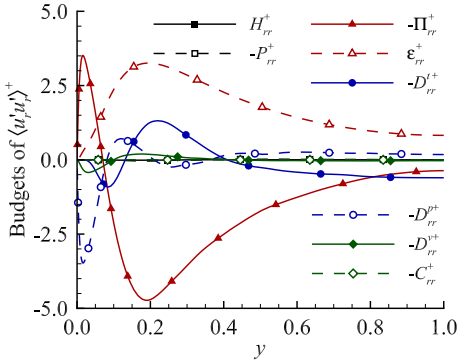

(a) Non-rotating pipe flow ($Ro_b = 0$)

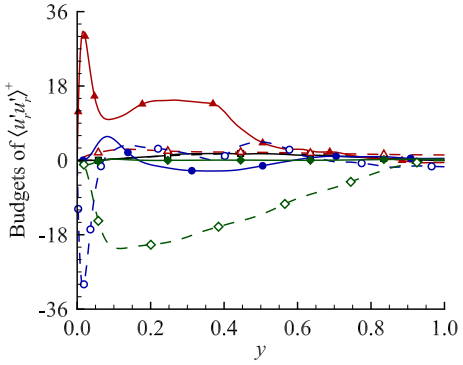

(b) Axially-rotating pipe flow ($Ro_b = 6$)

Figure 7. Budget balance of the radial Reynolds normal stress $\langle u_r' u_r' \rangle^+$ of the non-rotating ($Ro_b = 0$) and rotating ($Ro_b = 6$) flow cases. All budget terms are non-dimensionalized by u_τ^3/R.

axial direction, the Coriolis production term is zero identically for $\langle u_z' u_z' \rangle$. Therefore, we only analyze budget balance of $\langle u_r' u_r' \rangle$ and $\langle u_\beta' u_\beta' \rangle$ here, and the Coriolis production terms are $C_{rr} = 4\Omega_z \langle u_r' u_\beta' \rangle$ and $C_{\beta\beta} = -4\Omega_z \langle u_r' u_\beta' \rangle$, respectively.

As is shown in Fig. 7(a), the budget balance of $\langle u_r' u_r' \rangle^+$ is mostly dominated by $-\Pi_{rr}^+$, ε_{rr}^+ and $-D_{rr}^{p+}$ in the near-wall region of the pipe for the non-rotating pipe flow. Specifically, $-D_{rr}^{p+}$ and $-\Pi_{rr}^+$ behave as source terms in the inner region for $y \leq 0.071$ and in the outer region for $y \geq 0.071$, respectively. In contrast to the non-rotation pipe flow patterns shown in Fig. 7(a), it is apparent in Fig. 7(b) that the budget balance of $\langle u_r' u_r' \rangle^+$ is dominated by $-\Pi_{rr}^+$, $-D_{rr}^{p+}$ and $-C_{rr}$ at $Ro_b = 6$. Owing to the system rotation imposed, the Coriolis production term $-C_{rr}$ appears as a new source term which pumps a large amount of turbulence energy into $\langle u_r' u_r' \rangle^+$. The pressure-strain

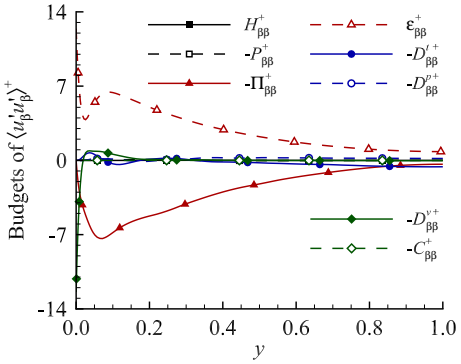

(a) Non-rotating pipe flow ($Ro_b = 0$)

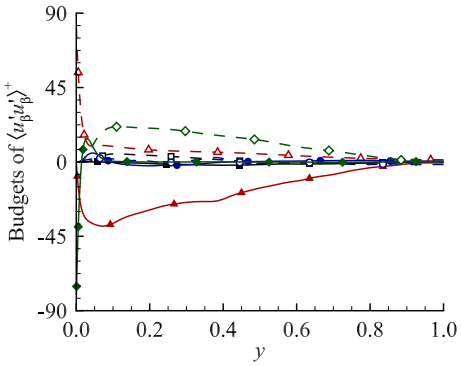

(b) Axially-rotating pipe flow ($Ro_b = 6$)

Figure 8. Budget balance of the azimuthal Reynolds normal stress $\langle u'_\beta u'_\beta \rangle^+$ of the non-rotating ($Ro_b = 0$) and rotating ($Ro_b = 6$) flow cases. All budget terms are non-dimensionalized by u_τ^3/R.

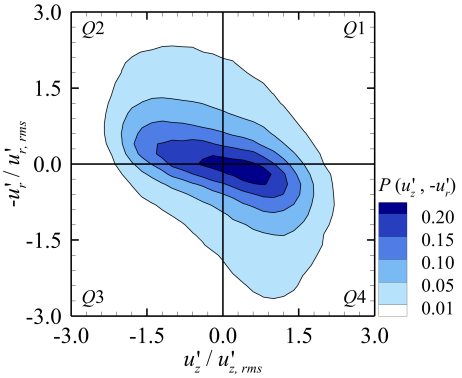

(a) Non-rotating pipe flow ($Ro_b = 0$)

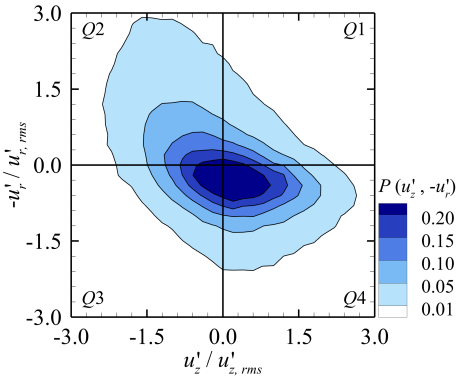

(b) Axially-rotating pipe flow ($Ro_b = 20$)

Figure 9. Contours of JPDF $P(u'_z\,,\,-u'_r)$ at wall-normal position $y^+ \approx 15$ of the pipe for the non-rotating ($Ro_b = 0$) and rotating ($Ro_b = 20$) flows. All contours have been split into four quadrants (Q) by black solid lines.

term functions completely as a sink term in the near-wall region up to $y = 0.872$. It is noticed that the peak values of $-\Pi^+_{rr}$ and $-D^{p+}_{rr}$ increase almost ninefold in the inner region compared with those of the non-rotating pipe flow.

Figure 8 compares budget balances of the azimuthal Reynolds normal stress $\langle u'_\beta u'_\beta \rangle^+$ of the non-rotating ($Ro_b = 0$) and rotating ($Ro_b = 6$) pipe flow cases. As is clear in Fig. 8(a), for the non-rotating pipe flow, the budget balance of $\langle u'_\beta u'_\beta \rangle^+$ is primarily dominated by $\varepsilon^+_{\beta\beta}$ and $-D^{v+}_{\beta\beta}$ in the inner region of the pipe. However, in the outer region, $-\Pi^+_{\beta\beta}$ and $\varepsilon^+_{\beta\beta}$ make primary contributions to $\langle u'_\beta u'_\beta \rangle^+$. The system rotation changes the budget balance of $\langle u'_\beta u'_\beta \rangle^+$ considerably. As is evident from Fig. 8(b), at $Ro_b = 6$, the Coriolis production term $-C_{\beta\beta}$ becomes the dominant sink term to balance with $-\Pi^+_{\beta\beta}$. By comparing Fig. 7(b) with Fig. 8(b), it is clear that the Coriolis production term is able to transfer turbulence energy from $\langle u'_\beta u'_\beta \rangle^+$ to $\langle u'_r u'_r \rangle^+$, simply because $C_{rr} \equiv -C_{\beta\beta}$.

Figure 9 compares contours of joint probability density function (JPDF) $P(u'_z\,,\,-u'_r)$ at the wall-normal position $y^+ \approx 15$ of the pipe for the non-rotating ($Ro_b = 0$) and rotating ($Ro_b = 20$) flows. To compare with the familiar turbulent plane-channel flows, the negative of the instantaneous radial velocity fluctuation u'_r is used here. In Figs. 9(a) and (b), the $Q2$ and $Q4$ quadrants relate to the ejection (featuring $u'_z < 0$ and $-u'_r > 0$) and sweeping (featuring $u'_z > 0$ and $-u'_r < 0$) events, respectively. It is evident that as the rotation number increases from $Ro_b = 0$ to 20, the ejection events tend to produce high intensities with a low probability, while the sweep events show an opposite trend. Lower intensities of the sweep events further result in a suppression in the formation of hairpin structures under the influence of the axial system rotation.

Figure 10 compares instantaneous streaky structures (demonstrated based on u'^+_z) in the β-z plane at the wall-normal position $y^+ \approx 15$ for the non-rotating ($Ro_b = 0$) and rotating ($Ro_b = 20$) flows. The axial domain is arbitrarily selected at $z/R \in [0, 10]$. In Fig. 10(a), the positively (indicated by red color) and negatively (indicated by blue color) fluctuating streaks alternate in the azimuthal direction in a non-rotating pipe flow. It is observed that the axial length scales of the negatively fluctuating streaks are apparently longer than those of the positively fluctuating streaks. By contrast, the azimuthal length scales of the positively fluctuating streaks are wider than those of the negatively fluctuating streaks. As shown in Fig. 10(b), at $Ro_b = 20$, the negatively fluctuating streaks are elongated along the axial direction. The period (or spacing between two adjacent negatively fluctuating streaks) becomes greater in the azimuthal direction in response to the system rotation imposed. It is also interesting to observe that the streaky structures are tilted, a physical feature that relates to the secondary flows shown previously in Fig. 2(b). In contrast with the negatively fluctuating streaks, a reduction on the positively fluctuating streaks is observed at $Ro_b = 20$. It indicates that axial system rotation tends to impede the formation of the hairpin structures by suppressing the sweep events and to laminarize the flow field which is consistent with the observation in Fig. 9(b).

Figure 11 compares instantaneous axial vorticity fluctuation (ω'^+_z) patterns in the β-z plane at $y^+ \approx 15$ for the non-rotating ($Ro_b = 0$) and rotating ($Ro_b = 20$) flows. For the non-rotating pipe flow shown in Fig. 11(a), numerous small-scale structures are seen in the β-z plane. However, in response to the axial system rotation, these small-scale turbulence structures are stretched along the axial direction at $Ro_b = 20$ and tilted slightly along the azimuthal direction, a pattern that is consistent with the observation of Fig. 10(b).

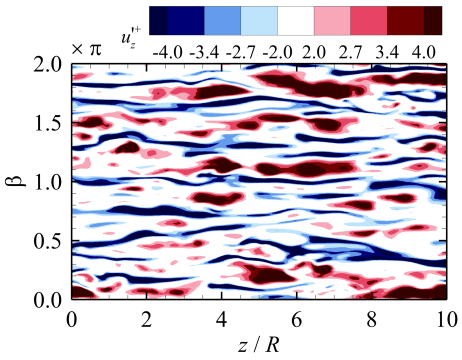

(a) Non-rotating pipe flow ($Ro_b = 0$)

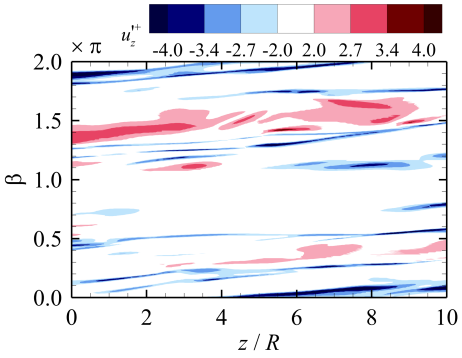

(b) Axially-rotating pipe flow ($Ro_b = 20$)

Figure 10. Contours of instantaneous axial velocity fluctuations ($u_z'^+$) in the β-z plane at wall-normal position $y^+ \approx 15$ for the non-rotating ($Ro_b = 0$) and rotating ($Ro_b = 20$) flows.

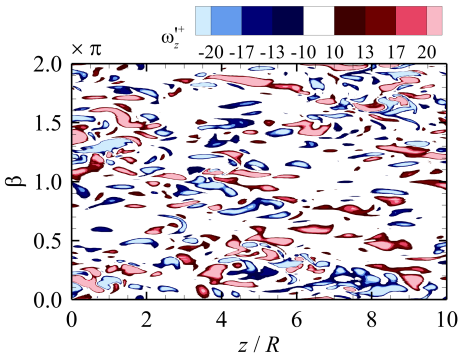

(a) Non-rotating pipe flow ($Ro_b = 0$)

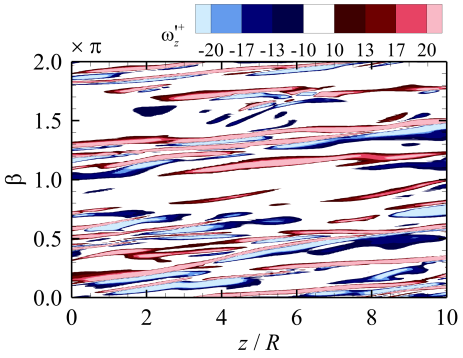

(b) Axially-rotating pipe flow ($Ro_b = 20$)

Figure 11. Contours of instantaneous axial vorticity fluctuations ($\omega_z'^+$) in the β-z plane at wall-normal position $y^+ \approx 15$ for the non-rotating ($Ro_b = 0$) and rotating ($Ro_b = 20$) flows.

CONCLUSIONS

Turbulent flow confined within a circular pipe subjected to axial rotation has been studied using DNS. To conduct a thorough investigation of the Coriolis force effect on the flow field, a wide range of rotation numbers varying from $Ro_b = 0$ to 20 have been tested. In response to the axial system rotation tested, secondary flow in form of a single counter-rotating vortex is induced at the pipe centre. As rotation number Ro_b increases, a maximum of $\langle u_z \rangle^+$ is observed at the pipe centre at $Ro_b = 6$. As Ro_b further increases above 6, the system rotation tends to weaken $\langle u_z \rangle^+$. It is also interesting that the peak position of the mean azimuthal velocity $r\langle u_\beta \rangle^+ / R$ is independent of Ro_b, which occurs at $y \approx 0.4$ where $\langle \omega_z \rangle^+$ is zero identically.

As the rotation number increases, the secondary flows adversely influence the magnitude of $\langle u_z' u_z' \rangle^+$ in the near-wall region and shift the $\langle u_z' u_z' \rangle^+$ peak towards the pipe centre. The values of $\langle u_r' u_r' \rangle^+$ and $\langle u_\beta' u_\beta' \rangle^+$ increase in most pipe regions but decrease when Ro_b goes beyond 14, making the dominant contributions to the TKE level of the flow. The magnitude of $k_z^+ \widetilde{E}_{zz}^+$ starts to decrease as soon as the axial rotation is imposed. This indicates that the axial rotation tends to suppress the strength of axial turbulent motions, and the characteristic wavelength of the axial turbulent structures enlarges as the axial system rotation speeds up.

It is observed that the Coriolis production and pressure-strain terms are the dominant terms in the budget balances of $\langle u_r' u_r' \rangle^+$ and $\langle u_\beta' u_\beta' \rangle^+$ in the outer region of the pipe under an axial system rotation. The function of the Coriolis force is to shift TKE between $\langle u_r' u_r' \rangle^+$ and $\langle u_\beta' u_\beta' \rangle^+$, simply because $C_{rr} = -C_{\beta\beta}$. In response to the system rotation imposed, the near-wall streaks extend in the streamwise direction and tilt in the azimuthal direction. It is observed that the magnitude of the positively fluctuating streaks in the rotating case is much smaller than that in the non-rotating case, indicating that the axial system rotation tends to suppress the sweep events to further restrain the formation of the hairpin structures, a trend that is further evidenced by the JPDF pattern of u_z' and -u_r'.

REFERENCES

Blackburn, H. M. & Sherwin, S. J. 2004 Formulation of a Galerkin spectral element-Fourier method for three-dimensional incompressible flows in cylindrical geometries. *J. Comp Phys.* **197** (2), 759–778.

Chin, C., Ooi, A. S. H., Marusic, I. & Blackburn, H. M. 2010 The influence of pipe length on turbulence statistics computed from direct numerical simulation data. *Phys. Fluids* **22** (11), 115107.

Eggels, J. G. M., Unger, F., Weiss, M. H., Westerweel, J., Adrian, R. J., Friedrich, R. & Nieuwstadt, F. T. M. 1994 Fully developed turbulent pipe flow: a comparison between direct numerical simulation and experiment. *J. Fluid Mech.* **268**, 175–210.

Orlandi, P. & Ebstein, D. 2000 Turbulent budgets in rotating pipes by DNS. *Int. J. Heat Fluid Flow* **21**, 499–505.

Orlandi, P. & Fatica, M. 1997 Direct simulations of turbulent flow in a pipe rotating about its axis. *J. Fluid Mech.* **343**, 43–72.

Reich, G. & Beer, H. 1989 Fluid flow and heat transfer in an axially rotating pipe - I. Effect of rotation on turbulent pipe flow. *Int. J. Heat Mass Transfer* **32** (3), 551–562.

Wu, X.-H. & Moin, P. 2008 A direct numerical simulation study on the mean velocity characteristics in turbulent pipe flow. *J. Fluid Mech.* **608**, 81–112.

Zhang, Z.-P. & Wang, B.-C. 2019 Direct numerical simulation of turbulent flow in a circular pipe subjected to radial system rotation. *Flow, Turbul. Combust.* **103** (4), 1057–1079.